

Deep Fusion Prior for Multi-Focus Images Super Resolution Fusion

Yuanjie Gu, Zhibo Xiao, Hailun Wang, Cheng Liu, and Shouyu Wang

Abstract—This paper unifies the multi-focus images fusion (MFIF) and blind super resolution (SR) problems as the multi-focus image super resolution fusion (MFISRF) task, and proposes a novel unified dataset-free unsupervised framework named deep fusion prior (DFP) to address such MFISRF task. DFP consists of SKIPnet network, DoubleReblur focus measurement tactic, decision embedding module and loss functions. In particular, DFP can obtain MFISRF only from two low-resolution inputs without any extent dataset. SKIPnet implementing unsupervised learning via deep image prior is an end-to-end generated network acting as the engine of DFP. DoubleReblur is used to determine the primary decision map without learning but based on estimated PSF and Gaussian kernel convolution. Decision embedding module optimizes the decision map via learning. DFP loss functions composed of content loss, joint gradient loss and gradient limit loss can obtain high-quality MFISRF results robustly. Experiments have proved that our proposed DFP approaches or even outperforms those state-of-art MFIF and SR method combinations. Additionally, DFP is a general framework, thus its networks and focus measurement tactics can be continuously updated to further improve the MFISRF performance. DFP codes are open source available at <http://github.com/GuYuanjie/DeepFusionPrior>.

Index Terms—Multi-focus image fusion, super resolution, unified model, unsupervised learning, dataset-free learning.

I. INTRODUCTION

THE majority of information acquisition, processing and analysis are based on visual perception system, which first records images, then distinguishes, recognizes and extracts targets, and finally analyzes them to provide instructions for system decision and control. Among them, image recording is the key premise for precision decision. But unfortunately, due to depth of field (DoF) and resolution limitations of optical systems, recorded images often suffer from resolution reduction and defocus blur, thus inevitably deteriorating the subsequent image processing and analysis. Therefore, in order to improve image quality, multi-focus image fusion (MFIF) and super-resolution (SR) methods have been adopted to extend the imaging DoF and enhance the imaging resolution, respectively.

Manuscript received xxxx xx, xxxx; revised xxxx xx, xxxx, accepted xxxx xx, xxxx. Date of publication xxxx xx, xxxx; date of current version xxxx xx, xxxx. This work was supported by National Natural Science Foundation of China (61705092) and Natural Science Foundation of Jiangsu Province of China (BK20170194). The associate editor coordinating the review of this manuscript and approving it for publication was Prof. xxx xx. (Corresponding author: Shouyu Wang.) Yuanjie Gu, Zhibo Xiao, Hailun Wang, Cheng Liu, and Shouyu Wang are with the Computational Optics Laboratory, School of Science, Jiangnan University, Wuxi, Jiangsu 214122, China (yuanjie_gu@stu.jiangnan.edu.cn; zhibo_xiao@stu.jiangnan.edu.cn; hailun_wang@stu.jiangnan.edu.cn; chengliu@siom.ac.cn; shouyu@jiangnan.edu.cn). Digital Object Identifier 10.1109/TCI.2022.xxxxxxx

For MFIF, methods can be roughly divided into two categories according to whether or not using deep learning. Most non-deep learning methods determine focus measurements and obtain decision maps to guide fusion. However, these decision maps suffer from disadvantages such as edge fragmentation and obvious transition. Supervised deep learning methods can obtain high-quality decision maps, but they rely on large handcrafted datasets. Unsupervised deep learning methods transform ground truths to features which can be obtained from inputs. Nevertheless, most of these features excessively rely on gradient, often leading to image edge deepening and painterly stylization. Besides, these unsupervised methods still require large datasets. For SR, interpolation-, example- and deep learning-based approaches are commonly used. Interpolation-based approaches only use pixel information of low-resolution image itself to interpolate pixel based on its surrounding, but their reconstruction results are often blurry. Example-based methods learn mapping between low- and high-resolution patches from internal or external datasets. While the feature extraction and mapping functions are still handcrafted, which inevitably limit high-frequency information learning. Supervised deep learning-based approaches reconstruct high-frequency information or fuse multi-scale information for resolution improvement. But unsupervised ones enhance resolution via generative adversarial game or iteration. Moreover, almost all the works deal with MFIF and SR separately. However, we find that MFIF and SR share a unified physical model. The imaging process can be described as

$$i(x, y) = h(x, y) * o(x, y) + n(x, y) \quad (1)$$

where $h(x, y)$ is the 2-D point spreading function (PSF), $o(x, y)$ is the object, $n(x, y)$ is the additive noise, $*$ is the spatial convolution, and $i(x, y)$ is the image. For SR, its purpose is to use $i(x, y)$ to obtain an estimate $\hat{o}(x, y)$ of the real object $o(x, y)$. While for MFIF, its model can be described in (2), where $i_f(x, y)$ and $i_b(x, y)$ are the unfused images focusing on foreground and background, $m_f(x, y)$ and $m_b(x, y)$ are the decision maps determining the foreground and background regions, E is the identity matrix, and $u(x, y)$ is the fused image.

$$u(x, y) = m_f(x, y) \cdot i_f(x, y) + m_b(x, y) \cdot i_b(x, y) \quad (2a)$$

$$m_f(x, y) + m_b(x, y) = E \quad (2b)$$

Both $i_f(x, y)$ and $i_b(x, y)$ can be represented by (3a) and (3b), in which $o_f(x, y)$ and $o_b(x, y)$ are the separated foreground and background objects from $o(x, y)$, and $h_f(x, y)$ and $h_d(x, y)$ are the 2-D focus and defocus PSFs.

$$i_f(x, y) = h_f(x, y) * o_f(x, y) + h_d(x, y) * o_b(x, y) + n_f(x, y) \quad (3a)$$

$$i_b(x, y) = h_d(x, y) * o_f(x, y) + h_f(x, y) * o_b(x, y) + n_b(x, y) \quad (3b)$$

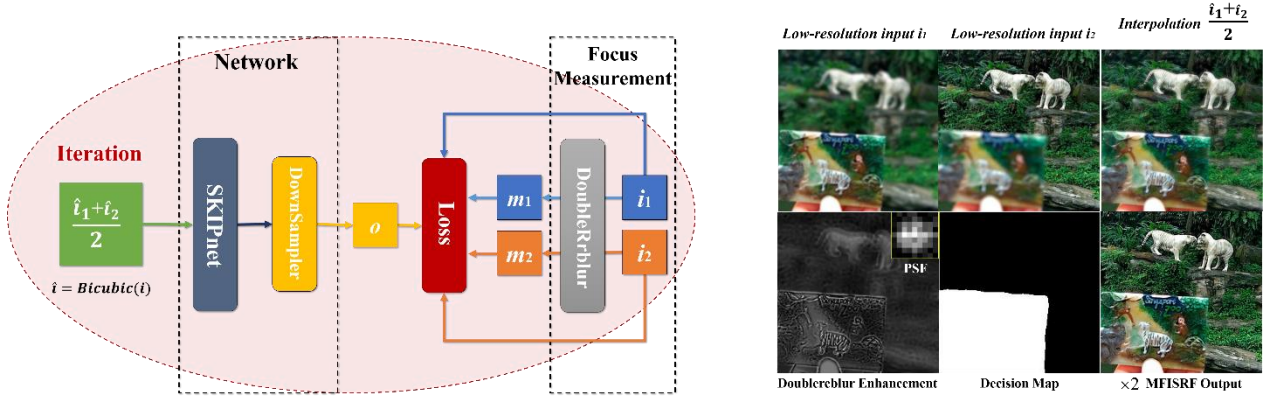


Fig. 1. Illustration of the key idea of DFP. i_1 is the foreground image, i_2 is the background image, $(\hat{i}_1 + \hat{i}_2)/2$ is the average of the interpolated foreground and background images, decision map can be obtained according to the DoubleReblur focus measurement tactic, and the output is the MFISRF result.

(4) can be obtained by substituting (3) into (2a), and it can be further generalized to (5).

$$u(x, y) = \left\{ \begin{aligned} &[m_f(x, y) \cdot h_f(x, y) + m_b(x, y) \cdot h_b(x, y)] * o_f(x, y) \\ &+ [m_f(x, y) \cdot h_d(x, y) + m_b(x, y) \cdot h_f(x, y)] * o_b(x, y) \end{aligned} \right\} \quad (4)$$

$$u(x, y) = \hat{h}(x, y) * o(x, y) + \hat{n}(x, y) \quad (5)$$

According to (2) to (5), for MFIF, its purpose is to use $i_f(x, y)$ and $i_b(x, y)$ to obtain the $\hat{o}(x, y)$ for image fusion. It reveals that MFIF and SR share the unified physical model. Therefore, MFIF and blind SR tasks can be combined as a multi-focus image super resolution fusion (MFISRF) task.

Here, we propose deep fusion prior (DFP), which implements MFIF and blind SR with unified, unsupervised, dataset-free and robust model to deal with the MFISRF task. DFP consists of SKIPnet network, DoubleReblur focus measurement tactic, decision embedding module and loss functions. In particular, SKIPnet implementing unsupervised learning via deep image prior is an end-to-end generated network acting as the engine of DFP. The core idea of DoubleReblur is to reblur the image via kernel convolution: the clear focus region becomes blurred, and the defocus region is still blurred. Therefore, the focus region can be determined according to difference between the reblurred and original images. Moreover, in order to enhance the performance, the estimated PSF and Gaussian kernels are both used as double reblur for focus measurement. Based on the DoubleReblur determined focus regions, decision map can be obtained using the largest region floorfill algorithm. The selectable learning-based map embedding is then used to optimize the decision map. The SKIPnet iteratively updates the parameters with invariable input, and the fused super resolution image is generated using loss functions to constrain solution space. The designed loss functions are composed of the content loss, the joint gradient loss and the gradient limit loss. The content loss is to constrain the SKIPnet to learn the clear region of each image. The joint gradient loss is to enhance the SKIPnet to learn the high-frequency information as well as to reduce the dependency of decision map. The gradient limit loss is to reduce the noise. All of these loss functions can guarantee high-quality MFISRF results robustly. Foremost, the main contributions of the proposed DFP are summarized as follows:

- *In theory*, we unify the MFIF and blind SR tasks as a **MFISRF** task to propose a new perspective for MFIF and SR.
- *In framework*, we design a **unified, dataset-free, unsupervised** and **robust** framework DFP to address the MFISRF task. DFP works with only one network for MFIF and SR. It is an unsupervised method without ground truth. Its fusion performance does not rely on the obtained decision map quality. Additionally, DFP is a general framework, thus its networks and focus measurement tactics can be continuously updated to further improve the MFISRF performance.
- *In performance*, we compare our DFP with the combinations of 12 MFIF methods and 3 SR methods on the latest MFI-WHU [1] benchmark dataset. Experiments have proved that our proposed DFP approaches or even outperforms those state-of-art MFIF and SR method combinations.

The paper is organized as follows. First, we review the related works on MFIF and SR in Section 2. Then, we introduce the details of DFP in Section 3. Next, we test the performance of DFP via comparing other reported works in Section 4. Finally, we discuss and conclude this work in Sections 5 and 6, respectively.

II. RELATED WORKS

A. MFIF Methods

For MFIF, methods can be classified into non-deep learning and deep learning types. In non-deep learning approaches, MFIF can be roughly summarized as an inverse process of extraction, and the key to these approaches lies in two important aspects: focus measurement and fusion rules. MFIF focus measurement can be implemented in either spatial domain or transform domain. There are mainly 3 tactics in focus measurement in spatial domain such as pixel-[2], [3], [4], [5], [6], [7], [8], block-[9] and region-based ones [10]. Although spatial domain methods can obtain focus measurement, they are not generalizable enough, focus measurement approaches in transform domain can improve the performance. There are mainly 5 tactics in focus measurement in transform domain such as sparse representation-based [11], [12], multi-scale-based [13], [14], [15], [16], [17], gradient-based [18], [19], feature-space-

based [20] and hybrid ones [21]. However, these transform domain methods are mostly based on Laplacian pyramid, gradient pyramid, discrete wavelet (DWT), discrete cosine (DCT), curvelet transform (CVT) and so on. These handcrafted focus measurement approaches make fusion methods complex, thus intensifying the difficulty of designing fusion rules. Meanwhile, these handcrafted focus measurement approaches also cause edge fragmentation, obvious transition and many other problems. Besides, fusion rules are determined based on focus measurement. The often used rules include maximum, minimum, addition, l1-norm, and so on. However, the limit choices of these handcrafted fusion rules produce a glass ceiling on the performance improvement even in some deep learning-based methods.

Deep learning-based MFIF can often obtain end-to-end fusion, since they use networks act as fusion rules. There are mainly two categories as supervised and unsupervised learning-based approaches. For the supervised category, CNN [22] is the first learning-based model realizing end-to-end MFIF. Subsequently, a series of CNNs are used in MFIF including DRPL [23], ECNN [24], IFCNN [25], MADCNN [26] and PCANet [27]. Although these supervised methods have good performance in MFIF, they highly rely on large handcrafted datasets. Moreover, handcrafted datasets often fail in real-world applications. Not relying on using handcrafted datasets, the unsupervised learning methods including FusionDN [28], GCF [29], SESF [30], MFF-GAN [1], PMGI [31] and U2Fusion [32] have been designed. However, because most of these unsupervised methods often try to sharpen the edges via object enhancement and gradient, the difference between fused image and ground truth is still significant. Besides, almost all of these methods still rely on large datasets to drive.

B. SR Methods

For SR, methods can be classified into interpolation-, example- and deep learning-based types. In these approaches, SR can be summarized as an ill-posed inverse process of imaging. The interpolation-based methods rely on sampling and interpolation, and these interpolation tactics include nearest-neighbor, bilinear, bicubic, Sinc, Lanczos and so on. These interpolation-based methods only use the pixel information of low-resolution image itself, and the pixel at each position is interpolated based on the information around such pixel, so the reconstructed images are significantly blurry.

The example-based methods exploit transposed convolution [33], [34], sub-pixel [35] or meta upscale [36] to learn the mapping between the low-resolution and high-resolution patches from internal [37], [38], [39], [40] or external [41] datasets. Although the internal dataset-based methods can improve the quality, it is difficult to learn high-frequency information and large textural variations, and significantly slow to learn. Moreover, the generated reconstruction images often have marked serration. Therefore, external dataset-based methods are used to replenish high frequency from external images. Although these external dataset-based methods are efficient, the feature extraction and mapping functions are handcrafted, which limit high-frequency information learning.

In order to overcome the limitations of above approaches, deep learning-based approaches are proposed. There are mainly two categories as supervised and unsupervised

learning-based approaches. Since Dong et al. [42] pioneered the first supervised deep learning-based single image SR approach, a lot of end-to-end CNNs [42], [43], [44], [45], [46], [47] have been designed to improve the SR quality, and the key to these approaches lies in two important aspects: network backbone [48], [49], [50], [51], [52], [53], [54] and upsampling order [57], [58], [59]. But almost all of these supervised deep learning-based approaches rely on the large datasets consisting of fixed-system low-resolution and high-resolution image pairs. Unsupervised SR approaches are mainly based on adversarial generative networks [60], [61], [62], thus they are not fully unsupervised and still rely on large datasets. Deep-image-prior [64] (DIP) shows that the structure of generator deep neural networks is sufficient to capture a great deal of image statistical prior. It only needs low-resolution image as inputs to reconstruct high-resolution image at any scale. Like TV norm [63], DIP is an effective handcrafted prior. It is fully unsupervised without any external datasets and performs well dealing with textured and focused goals, although, not well for defocus goals.

Up to now, there is still no unified model that can implement both MFIF and SR tasks with only one network. Besides, almost all of the supervised and unsupervised deep learning-based methods require large datasets for training in both MFIF and SR tasks. Therefore, according to our unified MFISRF model explained in Eqs. (2) to (5), a unified, dataset-free and unsupervised method for MFISRF task should be considered.

III. DEEP FUSION PRIOR

In this section, we introduce the details of our proposed DFP. Based on our unified MFISRF model, the unsurprised DFP consists of SKIPnet, DoubleReblur, decision embedding and loss functions, which are detailed illustrated in the following.

A. DFP Framework

From a Bayesian perspective, either MFIF or SR task can be represented by (6).

$$\hat{o}(x, y) = \arg \max_{o(x, y)} \log p[u(x, y) | o(x, y)] + \log p[o(x, y)] \quad (6)$$

where $\log p(u/o)$ represents the log-likelihood of observation u , and $\log p(o)$ furnishes the prior of real scene independently. Furthermore, (6) can also be formulated as the energy minimization function as follows:

$$\hat{o}(x, y) = \arg \min_{o(x, y)} \frac{1}{2\sigma^2} \|u(x, y) - \mathcal{T}[o(x, y)]\|^2 + \lambda \mathcal{R}[o(x, y)] \quad (7)$$

where $\frac{1}{2\sigma^2} \|u(x, y) - \mathcal{T}[o(x, y)]\|^2$ is a data term ensuring the solution according to the degradation process, and $\lambda \mathcal{R}[o(x, y)]$ is a regularization term with regularization parameter λ .

Generally, the supervised learning-based methods to solve (7) train an optimization of a loss function in a dataset composed of N image pairs including “single image SR as HR-LR $\{(y_i, x_i)\}_{i=1}^N$ ”, “multi-image SR as HR-LRs $\{(y_i, (x_{1i}, x_{2i}, \dots, x_{ni}))\}_{i=1}^N$ ” and “MFIF as fused-unfused $\{(y_i, (x_{1i}, x_{2i}, \dots, x_{ni}))\}_{i=1}^N$ ”. For “HR-LR”, the training process can be represented by (8a). While for “HR-LRs” and “fused-unfused”, the training process can be represented by (8b). In

> REPLACE THIS LINE WITH YOUR MANUSCRIPT ID NUMBER (DOUBLE-CLICK HERE TO EDIT) <

(8), Θ is the trainable parameters, and \mathcal{L} is the loss function. It is easy to note that “HR-LRs” is similar to “fused-unfused”. The difference between them is the label \hat{x}_i , which limits the solution space of the model.

$$\min_{\Theta} \sum_{i=1}^N \mathcal{L}(\hat{x}_i, x_i) \quad (8a)$$

$$\min_{\Theta} \sum_{i=1}^N \mathcal{L}[\hat{x}_i, (x_{1i}, x_{2i}, \dots, x_{ni})] \quad (8b)$$

Furthermore, the unsupervised learning-based methods to implement the “HR-LRs” and “fused-unfused” construct focus measurement τ for converting inputs $(x_{1i}, x_{2i}, \dots, x_{ni})$ to label \hat{x}_i . Even the ground truth of the real scene is impossible to be obtained directly. But we can still unify the MFIF and SR tasks as unsupervised MFISRF task as follows:

$$\min_{\Theta} \sum_{i=1}^N \mathcal{L}[\tau(x_{1i}, x_{2i}, \dots, x_{ni}), (x_{1i}, x_{2i}, \dots, x_{ni})] \quad (9)$$

According to (9), we use DFP deal with the MFISRF task. We formulate the MFISRF task as the unified unsurprised dataset-free model demonstrated by (10), where n is the random noise or the average of interpolations, x_1, x_2, \dots, x_n are the low-resolution multi-focus images inputs, τ is the focus measurement tactic and K is the number of iterations.

$$\min_{\Theta} \sum_{i=1}^K \mathcal{L}[\tau(x_1, x_2, \dots, x_n), n] \quad (10)$$

To solve the training optimization problem as (10), DFP consisting of SKIPnet network, DoubleReblur focus measurement tactic, decision embedding module and loss functions is adopted as shown in Fig. 2, and its core ideas are summarized as follows:

- We use the average interpolated low-resolution images or even the multi-channel 2-D random noise as input. The high-quality MFISRF image can be generated relying on the handcrafted focus measurement and the SKIPnet acting as adaptive fusion rules.
- We design DoubleReblur focus measurement tactic based on computational imaging, morphological image processing and graphics without learning.
- We propose the learning-based decision embedding module in order to optimize the decision map obtained from DoubleReblur focus measurement tactic. The decision embedding module is not indispensable, but the DFP performance will be better when considering it.
- We design DFP loss functions composed of content loss, joint gradient loss and gradient limit loss to obtain high-quality MFISRF results robustly.

For the whole DFP, we use Algorithm 1 for its description. Additionally, DFP is a general framework, thus its networks as SKIPnet and focus measurement tactics as DoubleReblur can be continuously updated to further improve the MFISRF performance.

B. SKIPnet Architecture

It is well-known that the encoder-decoder framework is effective for generative works. In addition, U-Net [65] structures have been proved excellent for tasks such as image generation and segmentation. However, in order to guarantee the image-to-image translation invariance, there is no padding before convolution in U-Net. Because of this, the

shape between input and output is imparity. Moreover, this imparity also influences on the feature concatenation. While the input in SKIPnet is the average interpolated low-resolution images or even the random noise, thus the generative relation between input and output is more important than translation invariance. Therefore, reflection paddings and 1×1 convolutions are adopted to keep the shape of feature map fixed. Leaky-ReLU activation function is also used to improve the SKIPnet. Note that this work focuses on proposing a powerful and flexible unsupervised MFISRF method without any dataset rather than proposing new generator network architecture. As a matter of fact, the similar architectures of autocoder network can be found in [64], [66].

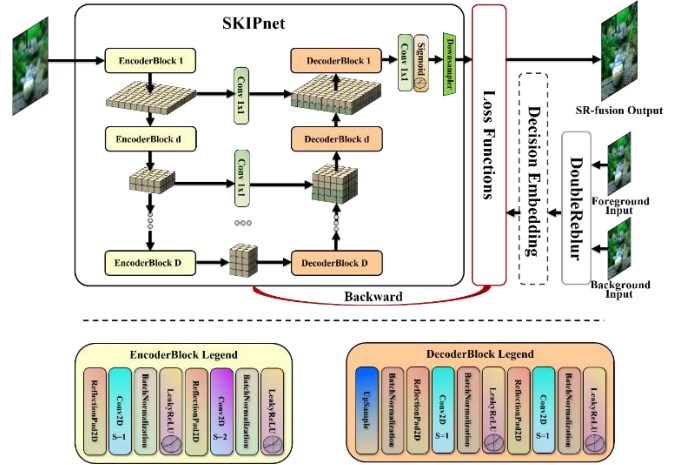


Fig. 2. DFP framework and SKIPnet architecture.

Algorithm 1 Deep Fusion Prior

- 1: Input: foreground input i_f , background input i_b .
Output \hat{i}_{MFISRF} .
- 2: **DoubleReblur**(i_f, i_b)
- 3: **Decision Embedding**
- 4: **for** iterations $K=1000$ **do**
- 5: Forward: $\hat{i}_{\text{MFISRF}} = \text{SKIPnet}(\text{input } n)$;
- 6: Select LANCZOS2 to downsample \hat{i}_{MFISRF} ;
- 7: $\mathcal{L} = \mathcal{L}_{\text{con}} + 0.5 \cdot \mathcal{L}_{j_grad} + 0.1 \cdot \mathcal{L}_{grad}$;
- 8: Backward to update SKIPnet parameters Θ ;
- 9: **end for**

The details of SKIPnet architecture is illustrated in Fig. 2. Based on the encoder-decoder framework, the SKIPnet is divided into the encoder and decoder parts, and they are symmetric about the central feature map ϕ_C . The backbone of the encoder part is composed of D encoder-blocks which extract feature maps in D scales. Each block consists of a reflection padding preparing layer, a 1-stride $n_d \times n_d$ convolution extracting layer, a batch normalization processing layer, a leaky-ReLU activating layer, a reflection padding preparing layer, a 2-stride $n_d \times n_d$ convolution downsampling layer, a batch normalization processing layer and a leaky-ReLU activating layer, successively. Identically, the backbone of the decoder part is composed of D decoder-blocks which extract and fuse feature maps in D scales. Each block consists of a bilinear upsampling layer, a batch normalization processing layer, a reflection padding

preparing layer, a 1-stride $n_d \times n_d$ convolution extracting layer, a batch normalization processing layer, a leaky-ReLU activating layer, a reflection padding preparing layer, a 1-stride $n_d \times n_d$ convolution extracting layer, a batch normalization processing layer and a leaky-ReLU activating layer, successively. For multi-scale feature map fusion, encoder feature maps $\phi_{v_d^o}(n)$ are concatenated to decoder feature maps $\phi_{u_d^o}(n)$. In the end, a 1×1 convolution is adopted to reduce dimensionality. A sigmoid activation function is adopted to obtain the demanded output format. In SKIPnet architecture, the downsampler with conventional approaches such as Bilinear, Bicubic and LANCZOS can be used to obtain the same size output as inputs, and the scale of the SR depends on the scale of the downsampler. Moreover, the depth D and the convolution kernel size n_d are adjustable. For convenient parameter adjustment, $D = 5$ and $n_d = 5$ are used in DFP, and two 3×3 convolution layers can be used to replace the 5×5 convolution layer for higher efficiency. Although some CNN based methods including ResNet [53], DenseNet [54] and Residual Dense Network [46] have been proved to work better on extracting features than autocoder architecture, they often have poor performance in image prior extraction. However, the image prior relying on handcrafted network architecture such as encoder-decoder still works well.

C. DoubleReblur

As we known, most MFIF methods [4], [5], [6], [7], [8], [10], [15], [22], [23] are based on decision maps, which can be obtained by handcrafted focus measurement. Therefore, combining with computational imaging, morphological image processing and graphics, we propose a DoubleReblur focus measurement model as shown in Fig. 3.

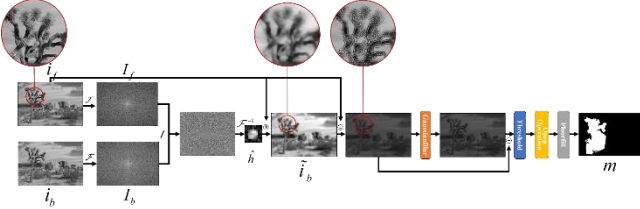


Fig. 3. DoubleReblur scheme

According to the imaging model in (1), the relation between the foreground input $g_f(x,y)$ and the background input $g_b(x,y)$ can be represented as (11).

$$i_b(x, y) = i_f(x, y) * h_s(x, y) + n_s(x, y) \quad (11)$$

To estimate the spread kernel $h_s(x,y)$, Fourier transform is implemented on both sides of (11) as follows:

$$\mathcal{F}\{i_b(x, y)\} = \mathcal{F}\{i_f(x, y) * h_s(x, y) + n_s(x, y)\} \quad (12a)$$

$$I_b(\xi, \eta) = I_f(\xi, \eta) \cdot H_s(\xi, \eta) + \mathcal{N}_s(\xi, \eta) \quad (12b)$$

where \mathcal{F} is the Fourier transform, $I_b(\xi, \eta)$, $I_f(\xi, \eta)$, $H_s(\xi, \eta)$ and $\mathcal{N}_s(\xi, \eta)$ are the frequency spectra of $i_b(x,y)$, $i_f(x,y)$, $h_s(x,y)$ and $n_s(x,y)$, respectively.

$$\frac{I_b(\xi, \eta)}{I_f(\xi, \eta)} = \frac{Y_f(\xi, \eta) \cdot H_s(\xi, \eta)}{Y_f(\xi, \eta)} + \frac{\mathcal{N}_s(\xi, \eta)}{G_f(\xi, \eta)} \quad (13)$$

To remove the noise term, a low-pass filter \mathcal{T} is performed on (13). In the end, the estimate of spread kernel $\hat{h}_s(x,y)$ can be obtained by follows:

$$\hat{h}_s(x, y) = \mathcal{F}^{-1} \left\{ \mathcal{T} \left\{ \frac{I_f(\xi, \eta)}{I_b(\xi, \eta)} - \frac{\mathcal{N}_s(\xi, \eta)}{I_f(\xi, \eta)} \right\} \right\} \quad (14)$$

The first reblur image can be obtained by (15).

$$\tilde{i}_b(x, y) = i_b(x, y) * \hat{h}_s(x, y) \quad (15)$$

Then, the Gaussian reblur \mathcal{G} as the second reblur is used to enhance the sharpness difference as $s(x,y)$ obtained by (16).

$$s(x, y) = |\tilde{i}_b(x, y) - \mathcal{G}\{\tilde{i}_b(x, y)\}| \quad (16)$$

$d(x,y)$ can be obtained by using threshold segmentation on sharpness difference image $s(x,y)$.

$$d(x, y) = \begin{cases} 1, & s(x, y) > t \\ 0, & s(x, y) \leq t \end{cases} \quad (17)$$

To eliminate gaps and holes, dilating and eroding are implemented as closed operation •

$$\hat{d}(x, y) = d(x, y) \bullet E \quad (18)$$

The decision map $m(x,y)$ can be finally obtained using the largest region floorfill algorithm.

$$m(x, y) = \mathcal{C}\{\hat{d}(x, y)\} \quad (19)$$

There are 5 parameters in DoubleReblur as $[k_g, k_d, k_e, t, f]$: k_g is the kernel size of Gaussian blur, k_d is the kernel size of dilating, k_e is the kernel size of eroding, t is the threshold of segmentation, and f is the bool flag control if the largest region filling is used. We transform the image to Y channel and use $[5, 3, 3, 0.01, 1]$ for most images and slightly adjust parameters for different image details.

D. Decision Embedding

Since the decision maps are obtained from handcrafted focus measurement, they suffer from disadvantages such as edge fragmentation and false determination. In order to optimize the handcrafted decision maps, learning-based decision embedding is designed as Fig. 4. The input is obtained by the average of low-resolution inputs but can also be replaced by random noise. The binarized decision map can be generated by SKIPnet. Moreover, we design a optimized loss function \mathcal{L}_{opt} as (20) to optimize the decision map via minimizing the difference between focus measurement regions and original low-resolution inputs.

$$\mathcal{L}_{opt} = \frac{1}{H \cdot W} \sum_i \sum_j \left| \hat{m}_{i,j} - m_{i,j} \right| + \left| \hat{m}_{i,j} \cdot I_{fore,i,j} - I_{fore,i,j} \right| + \left| (1 - \hat{m}_{i,j}) \cdot I_{back,i,j} - I_{back,i,j} \right| \quad (20)$$

where H and W are the height and width of the image, I_{fore} and I_{back} are the foreground and background low-resolution inputs, m is the handcrafted decision map obtained by DoubleReblur, \hat{m} is the optimized decision map generated by SKIPnet. Algorithm 2 briefly demonstrates the decision embedding process. The decision embedding module is not indispensable, but the DFP performance will be better when considering it.

> REPLACE THIS LINE WITH YOUR MANUSCRIPT ID NUMBER (DOUBLE-CLICK HERE TO EDIT) <

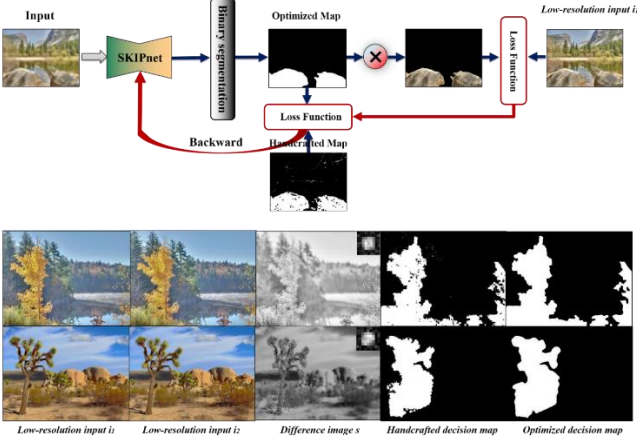


Fig. 4. Decision embedding scheme and examples.

Algorithm 2 Decision Embedding

```

1: Input: foreground input  $I_{fore}$ , background input  $I_{back}$ , input  $n$  and handcrafted decision map  $m$  which obtained by DoubleReblur;
   Output:  $\hat{m}$ ,  $1-\hat{m}$ .
2: for iterations  $K=500$  do
3:   Forward:  $\hat{m} = \text{SKIPnet}(\text{input } n)$ ;
4:   for  $x, y$  in  $\hat{m}$  do
5:     if  $\hat{m}(x,y) > 0.5$ ,  $\hat{m}(x,y)=1$ ;
6:     else  $\hat{m}(x,y)=0$ ;
7:   end for
8:    $\mathcal{L}_{opt} = \frac{1}{H \cdot W} \sum_i \sum_j |\hat{m}_{i,j} - m_{i,j}| + |\hat{m}_{i,j} \cdot I_{fore,i,j} - I_{fore,i,j}| + |(1-\hat{m}_{i,j}) \cdot I_{back,i,j} - I_{back,i,j}|$ 
9:   Backward to update SKIPnet parameters  $\Theta$ ;
10: end for

```

E. Loss Functions

The designed loss functions as (21) are composed of content loss \mathcal{L}_{con} , joint gradient loss \mathcal{L}_{j_grad} and gradient limit loss \mathcal{L}_{grad} . The content loss is to constrain the SKIPnet to learn the clear region of each image. The joint gradient loss is to enhance the SKIPnet to learn the high-frequency information and to reduce the dependency on decision maps. The gradient limit loss is to reduce the noise and oscillation effects. α , β and γ in (21) are weighted parameters, and set as 1, 0.5 and 0.1.

$$\mathcal{L} = \alpha \mathcal{L}_{con} + \beta \mathcal{L}_{j_grad} + \gamma \mathcal{L}_{grad} \quad (21)$$

$$\mathcal{L}_{con} = \frac{1}{H \cdot W} \sum_i \sum_j \lambda_1 \hat{m} \cdot \left| \hat{I}_{MFISRF_{i,j}} - I_{fore,i,j} \right| + \lambda_2 (1 - \hat{m}) \cdot \left| \hat{I}_{MFISRF_{i,j}} - I_{back,i,j} \right| \quad (22)$$

\mathcal{L}_{con} in (22) is the content loss, where λ_1 and λ_2 are weighted parameters both equal to 1. For generated MFISRF image \hat{I}_{MFISRF} , the focus regions in I_{fore} and I_{back} are obtained via decision maps. L_1 norms between the foreground focus region of \hat{I}_{MFISRF} and I_{fore} , and between the background focus region of \hat{I}_{MFISRF} and I_{back} are used to compute their distances. Rather than L_1 norm, L_2 norm has stronger penalty for large errors and weaker penalty for small errors, and ignores the effect of the image content itself. It is worth noting the human visual system (HVS) is especially sensitive to brightness and color changes in untextured areas of the

image. Moreover, [68] has proved that L_1 norm performs better than L_2 norm in SR tasks. So L_1 norm is adopted here.

$$\mathcal{L}_{j_grad} = \frac{1}{H \cdot W} \sum_i \sum_j \left| \nabla_L \hat{I}_{MFISRF_{i,j}} - \max(\nabla_L I_{fore,i,j}, \nabla_L I_{back,i,j}) \right| \quad (23)$$

\mathcal{L}_{j_grad} in (23) is the joint gradient loss, where ∇_L is the gradient obtained via Laplacian. The difference between focus and defocus regions is almost the high-frequency information. Moreover, the Laplacian gradient map can well describe high-frequency information. For MFIF, the maximal Laplacian gradient map of unfused inputs almost equals to the fused image. For SR, the Laplacian gradient map can provide more high-frequency details. Therefore, L_1 norm between the Laplacian gradient map of generated MFISRF image \hat{I}_{MFISRF} and the joint maximal Laplacian gradient map of low-resolution inputs I_{fore} and I_{back} is used to compute their distance.

$$\mathcal{L}_{grad} = \frac{1}{H \cdot W} \sum_i \sum_j (\nabla_x \hat{I}_{MFISRF_{i,j}} + \nabla_y \hat{I}_{MFISRF_{i,j}}) \quad (24)$$

\mathcal{L}_{grad} in (24) is the gradient limit loss. Unfortunately, DFP exploits the self-similarity property of input images themselves for reconstruction, thus inducing noise and oscillation. The gradient limit loss is used to reduce these noise and oscillation effects.

IV EXPERIMENTAL RESULTS

A. Qualitative Experimental Results

First, we qualitatively compare our proposed DFP with the combinations of learning-based MFIF (CNN [22], DRPL [23], ECNN [24], IFCNN [25], MADCNN [26], PCANet [27], FusionDN [28], GCF [29], SESF [30], MFF-GAN [1], PMGI [31], U2Fusion [32]) and conventional SR (Bicubic)/unsupervised SR (DIP [64])/supervised SR (SRCNN [41]). Methods relying on combinations of MFIF and SR work with two models and learn from large datasets. While our proposed DFP only works with one model and learns without any dataset.

Figs. 5 and 6 are the visual results of MFISRF $\times 2$ and $\times 4$ on MFI-WHU benchmark evaluation dataset [1]. In MFIF, CNN, DRPL, ECNN, IFCNN, MADCNN, PCANet and GCF provide similar results with almost discernible difference, but they all suffer from poor MFIF quality. PMGI improves the MFIF performance. It is compatible with multi-task such as infrared and visible image fusion, multi-exposure image fusion and medical image fusion. But these tasks are often in low contrast cases, so the PMGI results are often dark, blurred and edge enhanced. While SESF slightly improves the MFIF performance compared to PMGI by increasing the brightness and reducing the blur. FusionDN and its upgraded U2Fusion both compatible with multi-tasks have better MFIF performance than above methods. However, they still cannot completely solve problems such as dark, blurred and enhanced edge in MFIF. In SR, DIP improves image quality to some extent. But high-frequency details are lost especially in defocus and vista regions, since only self-similarity and low-level statistical priors are used. Although SRCNN performs better than DIP, it relies on training with large datasets which composed of fixed low- and high-resolution image pairs. Generally, it is easy to note

> REPLACE THIS LINE WITH YOUR MANUSCRIPT ID NUMBER (DOUBLE-CLICK HERE TO EDIT) <

that the unsupervised methods (FusionDN, GCF, SESF, MFF-GAN, PMGI) perform better than the supervised methods (CNN, DRPL, ECNN, IFCNN, MADCNN, PCANet) in MFIF. But contrarily, the supervised method (SRCNN) performs better than the unsupervised methods (Bicubic, DIP) in SR. Even DFP does not use any datasets for training, it still achieves high-quality results comparable to those obtained via the combinations of the unsupervised MFIF (FusionDN, GCF, SESF, MFF-GAN, PMGI, U2Fusion) and the supervised SR (SRCNN), proving the high performance of MFISRF when using our proposed method.



Fig. 5. We compare our approach against multiple state-of-the-art learning-based MFIF (CNN [22], DRPL [23], ECNN [24], IFCNN [25], MADCNN [26], PCANet [27], FusionDN [28], GCF [29], SESF [30], MFF-GAN [1], PMGI [31], U2Fusion [32]) and SR (Bicubic, DIP [64] and SRCNN [41]) in $\times 2$ condition on MFI-WHU 15.

B. Quantitative Experimental Results

Besides, quantitative comparisons are performed still using the MFI-WHU benchmark evaluation dataset [1]. The evaluation metrics include mean gradient (MG), edge intensity (EI), information entropy (IE), mean gray value (MGA) and polar edge coherence (ECO) [69], respectively. MG reflects the rate of contrast change of tiny details in the

image explained in (25a), in which H and W are the image height and width, ∇_x and ∇_y present the gradient in x- and y-directions, and I is the image.



Fig. 6. We compare our approach against multiple state-of-the-art learning-based MFIF (CNN [22], DRPL [23], ECNN [24], IFCNN [25], MADCNN [26], PCANet [27], FusionDN [28], GCF [29], SESF [30], MFF-GAN [1], PMGI [31], U2Fusion [32]) and SR (Bicubic, DIP [64] and SRCNN [41]) in $\times 4$ condition on MFI-WHU 01.

RMG describes the relative MG between ground truth (GT) and MFISRF as demonstrated in (25b).

$$MG = \frac{1}{H \cdot W} \sum_i \sum_j (\nabla_x I_{i,j} + \nabla_y I_{i,j}) \quad (25a)$$

$$RMG = \left| MG_{MFISRF} - \frac{MG_{GT}^1 + MG_{GT}^2}{2} \right| \quad (25b)$$

The most basic feature of an image is its edge existing between target and background, so it is one of the most important features to evaluate image fusion. EI is a quantitative coefficient to describe the edge information explained by (26a), in which s_x and s_y are the Sobel operators in x- and y-directions, and $*$ represents the convolution. RMG describes the relative EI between GT and MFISRF as demonstrated in (26b).

> REPLACE THIS LINE WITH YOUR MANUSCRIPT ID NUMBER (DOUBLE-CLICK HERE TO EDIT) <

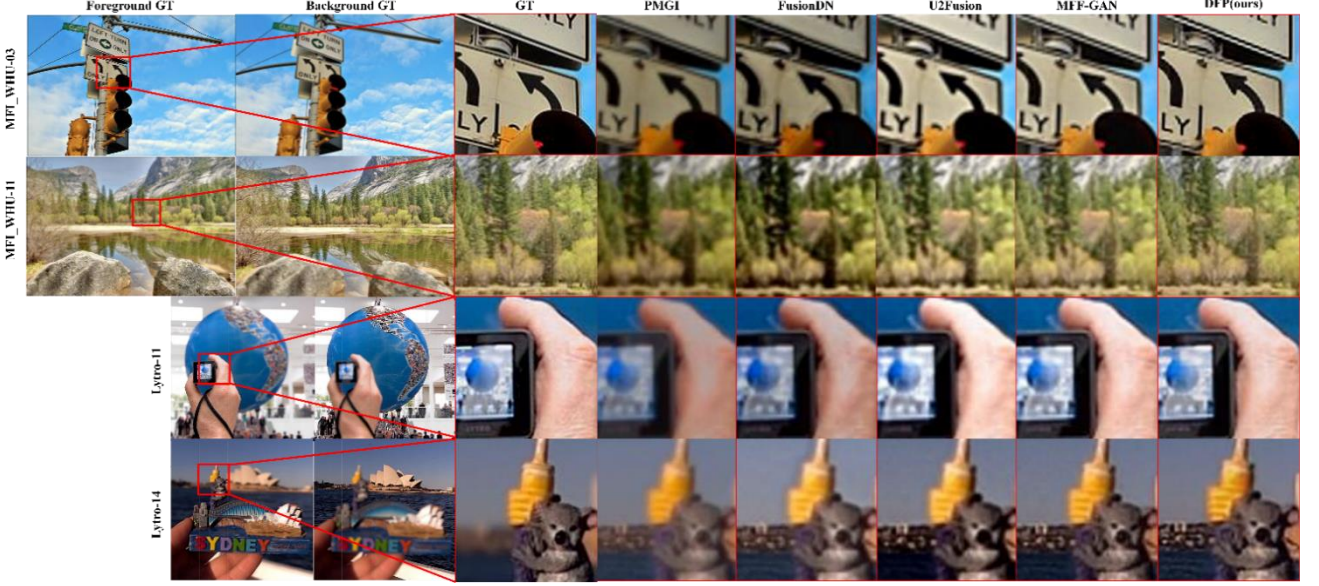


Fig. 7. We compare our approach against the combinations of FusionDN [28], MFF-GAN [1], PMGI [31], U2Fusion [32] and bicubic SR in $\times 2$ condition on MFI-WHU [1] and Lytro [67].

$$EI = \frac{1}{H \cdot W} \sqrt{\sum_i \sum_j [(I * s_x)^2 + (I * s_y)^2]} \quad (26a)$$

$$REI = \left| EI_{MFISRF} - \frac{EI_{GT}^1 + EI_{GT}^2}{2} \right| \quad (26b)$$

IE reflects the comprehensive characteristics of gray value at a pixel and its surrounding pixel gray distributions. It is demonstrated by (27a), where $f(i,j)$ is the frequency of occurrence of characteristic binary group. RIE describes the relative IE between GT and MFISRF as demonstrated in (27b).

$$IE = -\sum_i \sum_j \frac{f(i,j)}{H \cdot W} \lg \frac{f(i,j)}{H \cdot W} \quad (27a)$$

$$RIE = \left| IE_{MFISRF} - \frac{IE_{GT}^1 + IE_{GT}^2}{2} \right| \quad (27b)$$

MGA shown in (28a) is the average level of image gray, which represents the overall brightness level of the image. RIE describes the relative MGA between GT and MFISRF as demonstrated in (28b).

$$MGA = \frac{1}{H \cdot W} \sum_i \sum_j I_{i,j} \quad (28a)$$

$$RMGA = \left| MGA_{MFISRF} - \frac{MGA_{GT}^1 + MGA_{GT}^2}{2} \right| \quad (28b)$$

RECO reflects the edge similarity of the reconstructed and original images. It is illustrated in (29), where ECO is edge coherence according to [69], and C is a regularization constant. RECO describes the relative ECO between GT and MFISRF.

$$RECO = \left| 2 - \frac{ECO_{MFISRF} + C}{ECO_{GT}^{fore} + C} - \frac{ECO_{MFISRF} + C}{ECO_{GT}^{back} + C} \right| \quad (29)$$

We still compare our DFP with the combinations of 12 MFIF methods and 3 SR methods the same as above qualitative comparisons. 12 MFIF methods include 6 supervised

learning-based methods (CNN, DRPL, ECNN, IFCNN, MADCNN and PCANet) and 6 unsupervised

learning-based methods (FusionDN, GCF, SESF, MFF-GAN, PMGI and U2Fusion). 3 SR methods include conventional Bicubic, unsupervised learning-based DIP and supervised learning-based SRCNN. All methods except DIP are trained based on large datasets. However, DFP works without dataset.

Tables 1-3 quantitatively compare the performances using different MFIF and SR combined methods and the proposed MFISRF one according to above mentioned coefficients. Red, green and blue colors mark the 1st, 2nd and 3rd best of the performance. Our proposed MFISRF often can achieve high-quality super-resolved multi-focus fused images in both $\times 2$ and $\times 4$ conditions. Especially, even compared to the optimized combinations of unsupervised MFIF methods and supervised SR method, our proposed DFP could still obtain rather low RMG, REI, RIE, RMGA and RECO values very close to or even lower than those obtained by the optimized MFIF and SR combined methods.

V DISCUSSION

Still, many methods perform well in MFISRF such as FusionDN, MFF-GAN, PMGI and U2Fusion. Significantly, the difference between implementing MFISRF and MFIF with DFP is only downsampling, so the equivalent comparison should be DFP and the combination of unsupervised MFIF and interpolation SR. Here, extra $\times 2$ MFISRF results on MFI-WHU [1] and Lytro [67] obtained by DFP and the combinations of PMGI, FusionDN, U2Fusion, MFF-GAN and Bicubic interpolation are listed in Fig. 7. It is observed that the DFP results are very similar to the ground truth (GT) in all brightness, contrast, edge and color, and also much better than other competitors in both MFIF and SR quality. Especially, the results of FusionDN, MFF-GAN, PMGI and U2Fusion are excessively edge enhanced. The reason is that these methods are constructed with models and loss functions highly relied on gradients, both significantly improving image sharpness and visual perception but deviating from the ground truth. While DFP

> REPLACE THIS LINE WITH YOUR MANUSCRIPT ID NUMBER (DOUBLE-CLICK HERE TO EDIT) <

combines focus measurement and image prior to form an unsupervised closed-loop. Moreover, it also utilizes the weighted joint gradient loss to reduce the dependency of focus measurement. Therefore its results well balance the edge enhancement and image authenticity.

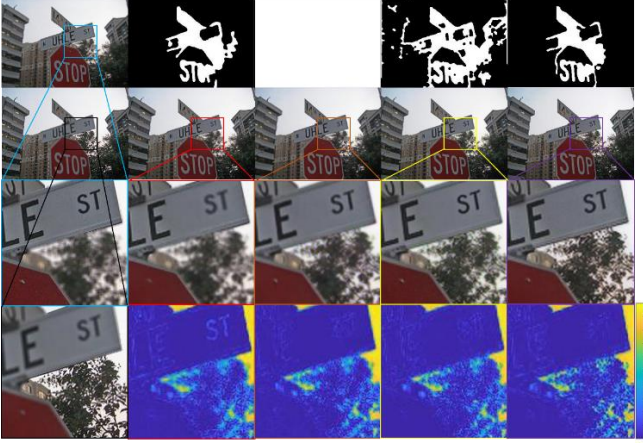


Fig. 8. We study the influence of decision map on both MFIF and SR performances. The first column images are the foreground and background ground truths. The second column results are obtained by DFP with the DoubleReblur parameter set as $[3,5,5,0.05,1]$ and without weighted joint gradient loss. The third, fourth and fifth column images are obtained by DFP but with different DoubleReblur parameter sets as $[3,5,5,0,1]$, $[3,5,5,0.01,1]$ and $[3,5,5,0.05,1]$, respectively. In these columns, the first image is the foreground decision map, the second image is the MFISRF image, the third one is the zoomed-in field-of-interest, and the last one is the pseudo-color image depicting the difference of ground truth and MFISRF result in Y channel.

Fig. 8 lists the results on MFI-WHU 29 to verify the DFP robustness. Images in the first column are the foreground and background ground truths. Results in the second column are obtained by DFP with the DoubleReblur parameter set as $[3,5,5,0.05,1]$ or without weighted joint gradient loss. The first image is the foreground decision map, the second image is the MFISRF image, the third one is the zoomed-in field-of-interest, and the last one is the pseudo-color image depicting the difference between ground truth and MFISRF result in Y channel. Identically, the images in the third, fourth and fifth columns are obtained by DFP but with different DoubleReblur parameter sets as $[3,5,5,0,1]$, $[3,5,5,0.01,1]$ and $[3,5,5,0.05,1]$, respectively. According to these results, it is proved that DFP has strong robustness since it can always provide high-quality MFIF results no matter the decision maps are good or bad. However, high-quality SR performance still depends on correct decision maps. Moreover, Fig. 9 reveals the convergence details of DFP and DIP still on the same MFI-WHU 29 with 3000 iterations. As DFP is multi-image SR while DIP is single-image SR, PSNR is less concerned here, while the convergence is more focused. According to the results, DFP converges only using ~ 400 iterations; however, DIP does not converge until ~ 2500 iterations. Additionally, DFP has a smoother trend with less fluctuations compared to DIP. Both results in Figs. 8 and 9 demonstrate the proposed DFP is robust in MFISRF tasks.

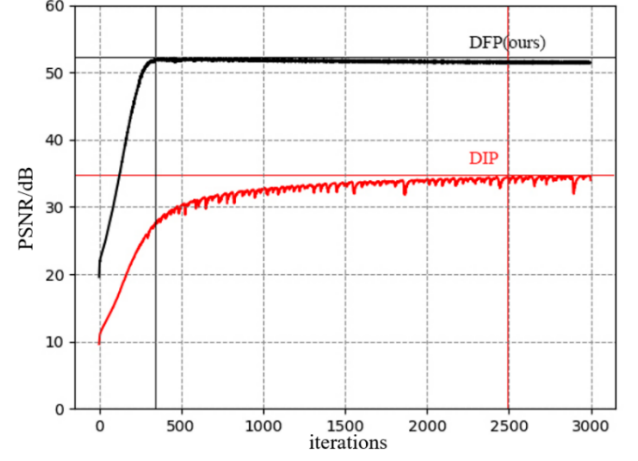


Fig 9. Convergence details of DFP and DIP on MFI-WHU 29 with 3000 iterations.

TABLE I

WE QUANTITATIVELY COMPARE OUR APPROACH AGAINST MULTIPLE STATE-OF-THE-ART LEARNING-BASED MFIF (CNN [22], DRPL [23], ECNN [24], IFCNN [25], MADCNN [26], PCANet [27], FUSIONDN [28], GCF [29], SESF [30], MFF-GAN [1], PMGI [31], U2FUSION [32]) AND BICUBIC SR IN $\times 2$ AND $\times 4$ CONDITIONS. RED, GREEN AND BLUE COLORS MARK THE 1ST, 2ND AND 3RD BEST OF THE PERFORMANCE.

	RMG	REI	RIE	RMGA	RECO
	$\times 2$ $\times 4$	$\times 2$ $\times 4$	$\times 2$ $\times 4$	$\times 2$ $\times 4$	$\times 2$ $\times 4$
CNN+	0.7207	3.6682	0.0176	0.1692	0.0844
BICUBIC	2.5906	22.7946	0.0598	0.1723	0.0488
DRPL+	0.6510	3.0538	0.0160	0.0883	0.0895
BICUBIC	2.5675	22.5395	0.0573	0.0957	0.0458
ECNN+	0.6724	3.2677	0.0171	0.1049	0.0725
BICUBIC	2.5747	22.6202	0.0580	0.1032	0.0363
IFCNN+	0.4649	1.8060	0.0151	0.5009	0.0261
BICUBIC	2.4400	21.1481	0.0535	0.4719	0.0102
MADCNN+	0.6525	3.0449	0.0158	0.1290	0.1046
BICUBIC	2.5562	22.4198	0.0572	0.1299	0.0602
PCANet+	0.7444	3.8778	0.0174	0.2240	0.0196
BICUBIC	2.6040	22.9440	0.0612	0.2252	0.0283
FusionDN+	0.9637	12.3182	0.3491	16.4175	0.0014
BICUBIC	1.7848	14.4899	0.3231	16.3919	0.0281
GCF+	0.6742	3.2527	0.0173	0.1370	0.1026
BICUBIC	2.5759	22.6316	0.0594	0.1271	0.0639
SESF+	0.7138	3.5747	0.0159	0.1735	0.0214
BICUBIC	2.5856	22.7406	0.0591	0.1686	0.0290
MFF-GAN+	0.5588	9.0613	0.1219	3.3443	0.0477
BICUBIC	2.0095	16.3748	0.0827	3.3727	0.0506
PMGI+	2.1311	18.4735	0.3899	18.1909	0.1422
BICUBIC	2.9701	27.0107	0.3921	18.1691	0.1434
U2FUSION+	0.9618	15.1490	0.2975	5.3168	0.0955
BICUBIC	1.3636	9.3573	0.2461	5.3213	0.1481
DFP (ours)	0.5840 1.8111	6.3614 14.8770	0.0222 0.0376	0.5324 0.5536	0.0056 0.0062

TABLE II

WE QUANTITATIVELY COMPARE OUR APPROACH AGAINST MULTIPLE STATE-OF-THE-ART LEARNING-BASED MFIF (CNN [22], DRPL [23], ECNN [24], IFCNN [25], MADCNN [26], PCANet [27], FusionDN [28], GCF [29], SESF [30], MFF-GAN [1], PMGI [31], U2Fusion [32]) AND UNSUPERVISED LEARNING-BASED SR (DIP [64]) IN $\times 2$ AND $\times 4$ CONDITIONS. RED, GREEN AND BLUE COLORS MARK THE 1ST, 2ND AND 3RD BEST OF THE PERFORMANCE.

METHOD	RMG	REI	RIE	RMGA	RECO
	$\times 2$ $\times 4$	$\times 2$ $\times 4$	$\times 2$ $\times 4$	$\times 2$ $\times 4$	$\times 2$ $\times 4$
CNN+	0.5780	2.6387	0.0310	0.3439	0.0863
DIP	2.0613	17.1756	0.0509	0.3378	0.0652
DRPL+	0.5019	2.4955	0.0297	0.4475	0.0884
DIP	2.0509	17.0586	0.0485	0.4205	0.0608
ECNN+	0.5301	2.3584	0.0310	0.4366	0.0690
DIP	2.0475	17.0193	0.0503	0.4090	0.0512
IFCNN+	0.3421	2.9407	0.0227	0.4985	0.0343
DIP	1.8643	15.0243	0.0447	0.3769	0.0064
MADCNN+	0.4957	2.2916	0.0310	0.4080	0.1036
DIP	2.0539	17.0954	0.0460	0.3769	0.0817
PCANet+	0.6014	2.7950	0.0288	0.2661	0.0192
DIP	2.0911	17.5025	0.0559	0.2713	0.0233
FusionDN+	1.1171	14.3756	0.3529	16.7732	0.0158
DIP	1.2079	9.5311	0.3429	16.7444	0.0317
GCF+	0.5141	2.5166	0.0276	0.4342	0.1009
DIP	2.0636	17.1856	0.0539	0.4224	0.0824
SESF+	0.5593	2.6525	0.0275	0.3503	0.0244
DIP	2.0534	17.0854	0.0474	0.3486	0.0245
MFF-GAN+	0.8850	12.7859	0.1358	3.1079	0.0585
DIP	1.8308	8.2245	0.1041	3.1314	0.0377
PMGI+	2.2334	19.5217	0.4057	18.5801	0.1329
DIP	2.6718	24.0968	0.4118	18.5721	0.1468
U2Fusion+	1.1756	17.2388	0.2929	5.2692	0.0940
DIP	0.5697	3.9655	0.2739	5.3012	0.1389
DFP (ours)	0.5840	6.3614	0.0222	0.5324	0.0056
	1.8111	14.8770	0.0376	0.5536	0.0062

TABLE III

WE QUANTITATIVELY COMPARE OUR APPROACH AGAINST MULTIPLE STATE-OF-THE-ART LEARNING-BASED MFIF (CNN [22], DRPL [23], ECNN [24], IFCNN [25], MADCNN [26], PCANet [27], FusionDN [28], GCF [29], SESF [30], MFF-GAN [1], PMGI [31], U2Fusion [32]) AND SUPERVISED LEARNING-BASED SR (SRCNN [41]) IN $\times 2$ AND $\times 4$ CONDITIONS. RED, GREEN AND BLUE COLORS MARK THE 1ST, 2ND AND 3RD BEST OF THE PERFORMANCE.

METHOD	RMG	REI	RIE	RMGA	RECO
	$\times 2$ $\times 4$	$\times 2$ $\times 4$	$\times 2$ $\times 4$	$\times 2$ $\times 4$	$\times 2$ $\times 4$
CNN+	0.7995	9.9926	0.0237	0.9516	0.0827
SRCNN	1.7145	13.6249	0.0317	0.7879	0.0705
DRPL+	0.9117	11.0625	0.0261	1.0490	0.0883
SRCNN	1.6749	13.1979	0.0290	0.8682	0.0695
ECNN+	0.8786	10.7192	0.0259	1.0448	0.0692
SRCNN	1.6891	13.3493	0.0303	0.8679	0.0598
IFCNN+	1.0715	13.0042	0.0355	1.5993	0.0378
SRCNN	1.4554	10.8233	0.0240	1.4270	0.0092
MADCNN+	0.8807	10.8249	0.0265	1.0127	0.1025
SRCNN	1.6566	13.0050	0.0283	0.8423	0.0834
PCANet+	0.7987	9.7746	0.0235	0.8760	0.0133
SRCNN	1.7302	13.7981	0.0341	0.7250	0.0082
FusionDN+	1.8200	22.2081	0.3592	17.1748	0.0138
SRCNN	0.9588	8.5307	0.3476	17.0702	0.0312
GCF+	0.8737	0.0241	10.6861	0.0241	0.0968
SRCNN	1.6905	13.3631	0.0311	0.8797	0.0864
SESF+	0.8097	10.1118	0.0249	0.9539	0.0153
SRCNN	1.7054	13.5246	0.0316	0.7985	0.0095
MFF-GAN+	2.2016	24.7978	0.1562	2.9512	0.0651
SRCNN	0.8676	5.2269	0.1060	2.9792	0.0338
PMGI+	1.7301	15.1158	0.3925	19.0188	0.1293
SRCNN	2.4111	21.4495	0.3913	18.9211	0.1447
U2Fusion+	2.1945	26.6641	0.3184	5.3172	0.0778
SRCNN	0.4994	6.2283	0.2815	5.3075	0.1156
DFP (ours)	0.5840	6.3614	0.0222	0.5324	0.0056
	1.8111	14.8770	0.0376	0.5536	0.0062

VI. CONCLUSION

In this study, we unify the MFIF and blind SR problems as the MFISRF task, and propose a novel unified dataset-free unsupervised framework DFP to address such MFISRF task. DFP consists of our designed SKIPnet end-to-end generated network to implement unsupervised learning via deep image prior, DoubleReblur tactic for focus measurement based on estimated PSF and Gaussian kernel convolution, decision embedding learned module for decision map optimization, and loss functions to guarantee high-quality MFISRF results robustly. Compared to 12 MFIF and 3 SR method combinations including both supervised and unsupervised ones, the proposed unsupervised dataset-free DFP approaches or even outperforms these state-of-art MFIF and SR method combinations. Furthermore, DFP is a general framework, thus its networks and focus measurement tactics can be continuously updated to further improve the MFISRF performance. We believe DFP can be potentially used in various computational photography applications.

ACKNOWLEDGMENT

This work was supported by National Natural Science Foundation of China (61705092); Natural Science Foundation of Jiangsu Province of China (BK20170194).

REFERENCES

- [1] H. Zhang, Z. Le, Z. Shao, H. Xu, and J. Ma, "MFF-GAN: An unsupervised generative adversarial network with adaptive and gradient joint constraints for multi-focus image fusion," *Inf. Fusion*, vol. 66, no. September 2020, pp. 40–53, 2021, doi: 10.1016/j.inffus.2020.08.022.
- [2] J. Tian, L. Chen, L. Ma, and W. Yu, "Multi-focus image fusion using a bilateral gradient-based sharpness criterion," *Opt. Commun.*, vol. 284, no. 1, pp. 80–87, 2011, doi: 10.1016/j.optcom.2010.08.085.
- [3] B. K. Shreyamsha Kumar, "Image fusion based on pixel significance using cross bilateral filter," *Signal, Image Video Process.*, vol. 9, no. 5, pp. 1193–1204, 2015, doi: 10.1007/s11760-013-0556-9.
- [4] Y. Liu, S. Liu, and Z. Wang, "Multi-focus image fusion with dense SIFT," *Inf. Fusion*, vol. 23, pp. 139–155, 2015, doi: 10.1016/j.inffus.2014.05.004.
- [5] X. Qiu, M. Li, L. Zhang, and X. Yuan, "Guided filter-based multi-focus image fusion through focus region detection," *Signal Process. Image Commun.*, vol. 72, no. December 2018, pp. 35–46, 2019, doi: 10.1016/j.image.2018.12.004.
- [6] S. Li, X. Kang, J. Hu, and B. Yang, "Image matting for fusion of multi-focus images in dynamic scenes," *Inf. Fusion*, vol. 14, no. 2, pp. 147–162, 2013, doi: 10.1016/j.inffus.2011.07.001.
- [7] J. Ma, Z. Zhou, B. Wang, and M. Dong, "Multi-focus image fusion based on multi-scale focus measures and generalized random walk," *Chinese Control Conf. CCC*, no. 1, pp. 5464–5468, 2017, doi: 10.23919/ChiCC.2017.8028223.
- [8] J. Ma, Z. Zhou, B. Wang, L. Miao, and H. Zong, "Multi-focus image fusion using boosted random walks-based algorithm with two-scale focus maps," *Neurocomputing*, vol. 335, pp. 9–20, 2019, doi: 10.1016/j.neucom.2019.01.048.
- [9] X. Bai, Y. Zhang, F. Zhou, and B. Xue, "Quadtree-based multi-focus image fusion using a weighted focus-measure," *Inf. Fusion*, vol. 22, pp. 105–118, 2015, doi: 10.1016/j.inffus.2014.05.003.
- [10] Y. Zhang, X. Bai, and T. Wang, "Boundary finding based multi-focus image fusion through multi-scale morphological focus-measure," *Inf. Fusion*, vol. 35, pp. 81–101, 2017, doi: 10.1016/j.inffus.2016.09.006.
- [11] Y. Liu and Z. Wang, "Simultaneous image fusion and denoising with adaptive sparse representation," *IET Image Process.*, vol. 9, no. 5, pp. 347–357, 2015, doi: 10.1049/iet-ipr.2014.0311.
- [12] Y. Liu, X. Chen, R. K. Ward, Z. J. Wang, and S. Member, "Sparse Representation," *Comput. Vis.*, vol. 23, no. 12, pp. 748–748, 2014, doi: 10.1007/978-0-387-31439-6_100096.
- [13] M. Amin-Naji and A. Aghagolzadeh, "Multi-Focus Image Fusion in DCT Domain using Variance and Energy of Laplacian and

- Correlation Coefficient for Visual Sensor Networks,” *J. AI Data Min.*, vol. 6, no. 2, pp. 233–250, 2018, doi: 10.22044/JADM.2017.5169.1624.
- [14] W. Z. Liu Yu, “Multi-focus image fusion based on wavelet transform and adaptive block,” *J. image Graph.*, vol. 8, no. 11, pp. 1435–1444, 2013.
- [15] S. Li, X. Kang, and J. Hu, “Image fusion with guided filtering,” *IEEE Trans. Image Process.*, vol. 22, no. 7, pp. 2864–2875, 2013, doi: 10.1109/TIP.2013.2244222.
- [16] D. P. Bavirisetti, G. Xiao, J. Zhao, R. Dhuli, and G. Liu, “Multi-scale Guided Image and Video Fusion: A Fast and Efficient Approach,” *Circuits, Syst. Signal Process.*, vol. 38, no. 12, pp. 5576–5605, 2019, doi: 10.1007/s00034-019-01131-z.
- [17] M. Amin-Naji, P. Ranjbar-Noiey, and A. Aghagolzadeh, “Multi-focus image fusion using Singular Value Decomposition in DCT domain,” *Iran. Conf. Mach. Vis. Image Process. MVIP*, vol. 2017–November, pp. 45–51, 2018, doi: 10.1109/IranianMVIP.2017.8342367.
- [18] S. Paul, I. S. Sevcenco, and P. Agathoklis, “Multi-exposure and multi-focus image fusion in gradient domain,” *J. Circuits, Syst. Comput.*, vol. 25, no. 10, pp. 1–18, 2016, doi: 10.1142/S0218126616501231.
- [19] Z. Zhou, S. Li, and B. Wang, “Multi-scale weighted gradient-based fusion for multi-focus images,” *Inf. Fusion*, vol. 20, no. 1, pp. 60–72, 2014, doi: 10.1016/j.inffus.2013.11.005.
- [20] H. Li, L. Li, and J. Zhang, “Multi-focus image fusion based on sparse feature matrix decomposition and morphological filtering,” *Opt. Commun.*, vol. 342, pp. 1–11, 2015, doi: 10.1016/j.optcom.2014.12.048.
- [21] Y. Liu, S. Liu, and Z. Wang, “A general framework for image fusion based on multi-scale transform and sparse representation,” *Inf. Fusion*, vol. 24, pp. 147–164, 2015, doi: 10.1016/j.inffus.2014.09.004.
- [22] Y. Liu, X. Chen, H. Peng, and Z. Wang, “Multi-focus image fusion with a deep convolutional neural network,” *Inf. Fusion*, vol. 36, pp. 191–207, 2017, doi: 10.1016/j.inffus.2016.12.001.
- [23] J. Li *et al.*, “DRPL: Deep Regression Pair Learning for Multi-Focus Image Fusion,” *IEEE Trans. Image Process.*, vol. 29, pp. 4816–4831, 2020, doi: 10.1109/TIP.2020.2976190.
- [24] M. Amin-Naji, A. Aghagolzadeh, and M. Ezoji, “Ensemble of CNN for multi-focus image fusion,” *Inf. Fusion*, vol. 51, no. August 2018, pp. 201–214, 2019, doi: 10.1016/j.inffus.2019.02.003.
- [25] Y. Zhang, Y. Liu, P. Sun, H. Yan, X. Zhao, and L. Zhang, “IFCNN: A general image fusion framework based on convolutional neural network,” *Inf. Fusion*, vol. 54, no. August 2018, pp. 99–118, 2020, doi: 10.1016/j.inffus.2019.07.011.
- [26] R. Lai, Y. Li, J. Guan, and A. Xiong, “Multi-Scale Visual Attention Deep Convolutional Neural Network for Multi-Focus Image Fusion,” *IEEE Access*, vol. 7, pp. 114385–114399, 2019, doi: 10.1109/ACCESS.2019.2935006.
- [27] X. Song and X. W. B. *Multimodal Pattern Recognition of Social Signals in Human-Computer-Interaction - 5th {IAPR} {TC} 9 Workshop, {MPRSS} 2018, Beijing, China, August 20, 2018, Revised Selected Papers*, vol. 11377. Springer International Publishing, 2019.
- [28] H. Xu, J. Ma, Z. Le, J. Jiang, and X. Guo, “FusionDN: A unified densely connected network for image fusion,” *AAAI 2020 - 34th AAAI Conf. Artif. Intell.*, pp. 12484–12491, 2020, doi: 10.1609/aaai.v34i07.6936.
- [29] H. Xu, F. Fan, H. Zhang, Z. Le, and J. Huang, “A Deep Model for Multi-Focus Image Fusion Based on Gradients and Connected Regions,” *IEEE Access*, vol. 8, pp. 26316–26327, 2020, doi: 10.1109/ACCESS.2020.2971137.
- [30] B. Ma, Y. Zhu, X. Yin, X. Ban, H. Huang, and M. Mukeshimana, “SESF-Fuse: an unsupervised deep model for multi-focus image fusion,” *Neural Comput. Appl.*, vol. 33, no. 11, pp. 5793–5804, 2021, doi: 10.1007/s00521-020-05358-9.
- [31] H. Zhang, H. Xu, Y. Xiao, X. Guo, and J. Ma, “Rethinking the Image Fusion: A Fast Unified Image Fusion Network based on Proportional Maintenance of Gradient and Intensity,” 2020.
- [32] H. Xu, J. Ma, J. Jiang, X. Guo, and H. Ling, “U2Fusion: A Unified Unsupervised Image Fusion Network,” *IEEE Trans. Pattern Anal. Mach. Intell.*, vol. 8828, no. c, pp. 1–1, 2020, doi: 10.1109/tpami.2020.3012548.
- [33] M. D. Zeiler, D. Krishnan, G. W. Taylor, and R. Fergus, “Deconvolutional networks,” *Proc. IEEE Comput. Soc. Conf. Comput. Vis. Pattern Recognit.*, pp. 2528–2535, 2010, doi: 10.1109/CVPR.2010.5539957.
- [34] F. B. M. Suah, “Preparation and characterization of a novel Co(II) optode based on polymer inclusion membrane,” *Anal. Chem. Res.*, vol. 12, pp. 40–46, 2017, doi: 10.1016/j.ancr.2017.02.001.
- [35] W. Shi *et al.*, “Real-Time Single Image and Video Super-Resolution Using an Efficient Sub-Pixel Convolutional Neural Network,” *Proc. IEEE Comput. Soc. Conf. Comput. Vis. Pattern Recognit.*, vol. 2016–December, pp. 1874–1883, 2016, doi: 10.1109/CVPR.2016.207.
- [36] X. Hu, H. Mu, X. Zhang, Z. Wang, T. Tan, and J. Sun, “Meta-SR: A magnification-arbitrary network for super-resolution,” *Proc. IEEE Comput. Soc. Conf. Comput. Vis. Pattern Recognit.*, vol. 2019–June, pp. 1575–1584, 2019, doi: 10.1109/CVPR.2019.00167.
- [37] G. Freedman and R. Fattal, “Image and video upscaling from local self-examples,” *ACM Trans. Graph.*, vol. 30, no. 2, 2011, doi: 10.1145/1944846.1944852.
- [38] C. Y. Yang, J. Bin Huang, and M. H. Yang, “Exploiting self-similarities for single frame super-resolution,” *Lect. Notes Comput. Sci. (including Subser. Lect. Notes Artif. Intell. Lect. Notes Bioinformatics)*, vol. 6494 LNCS, no. PART 3, pp. 497–510, 2011, doi: 10.1007/978-3-642-19318-7_39.
- [39] D. Glasner, S. Bagon, and M. Irani, “Super-resolution from a single image,” *Proc. IEEE Int. Conf. Comput. Vis.*, no. Iccv, pp. 349–356, 2009, doi: 10.1109/ICCV.2009.5459271.
- [40] K. I. Kim and Y. Kwon, “Single-image super-resolution using sparse regression and natural image prior,” *IEEE Trans. Pattern Anal. Mach. Intell.*, vol. 32, no. 6, pp. 1127–1133, 2010, doi: 10.1109/TPAMI.2010.25.
- [41] C. Dong, C. C. Loy, K. He, and X. Tang, “Image Super-Resolution Using Deep Convolutional Networks,” *IEEE Trans. Pattern Anal. Mach. Intell.*, vol. 38, no. 2, pp. 295–307, 2016, doi: 10.1109/TPAMI.2015.2439281.
- [42] J. Kim, J. K. Lee, and K. M. Lee, “Deeply-recursive convolutional network for image super-resolution,” *Proc. IEEE Comput. Soc. Conf. Comput. Vis. Pattern Recognit.*, vol. 2016–December, pp. 1637–1645, 2016, doi: 10.1109/CVPR.2016.181.
- [43] W. S. Lai, J. Bin Huang, N. Ahuja, and M. H. Yang, “Deep laplacian pyramid networks for fast and accurate super-resolution,” *Proc. - 30th IEEE Conf. Comput. Vis. Pattern Recognition, CVPR 2017*, vol. 2017–January, pp. 5835–5843, 2017, doi: 10.1109/CVPR.2017.618.
- [44] C. Ledig *et al.*, “Photo-realistic single image super-resolution using a generative adversarial network,” *Proc. - 30th IEEE Conf. Comput. Vis. Pattern Recognition, CVPR 2017*, vol. 2017–January, pp. 105–114, 2017, doi: 10.1109/CVPR.2017.19.
- [45] B. Lim, S. Son, H. Kim, S. Nah, and K. M. Lee, “Enhanced Deep Residual Networks for Single Image Super-Resolution,” *IEEE Comput. Soc. Conf. Comput. Vis. Pattern Recognit. Work.*, vol. 2017–July, pp. 1132–1140, 2017, doi: 10.1109/CVPRW.2017.151.
- [46] Y. Zhang, Y. Tian, Y. Kong, B. Zhong, and Y. Fu, “Residual Dense Network for Image Super-Resolution,” *Proc. IEEE Comput. Soc. Conf. Comput. Vis. Pattern Recognit.*, pp. 2472–2481, 2018, doi: 10.1109/CVPR.2018.00262.
- [47] W. Han, S. Chang, D. Liu, M. Yu, M. Witbrock, and T. S. Huang, “Image Super-Resolution via Dual-State Recurrent Networks,” *Proc. IEEE Comput. Soc. Conf. Comput. Vis. Pattern Recognit.*, pp. 1654–1663, 2018, doi: 10.1109/CVPR.2018.00178.
- [48] Y. LeCun, L. Bottou, Y. Bengio, and P. Haffner, “Gradient-based learning applied to document recognition,” *Proc. IEEE*, vol. 86, no. 11, pp. 2278–2323, 1998, doi: 10.1109/5.726791.
- [49] T. F. Gonzalez, “Handbook of approximation algorithms and metaheuristics,” *Handb. Approx. Algorithms Metaheuristics*, pp. 1–1432, 2007, doi: 10.1201/9781420010749.
- [50] K. Simonyan and A. Zisserman, “Very deep convolutional networks for large-scale image recognition,” *3rd Int. Conf. Learn. Represent. ICLR 2015 - Conf. Track Proc.*, pp. 1–14, 2015.
- [51] C. Szegedy *et al.*, “Going deeper with convolutions,” *Proc. IEEE Comput. Soc. Conf. Comput. Vis. Pattern Recognit.*, vol. 07–12–June–2015, pp. 1–9, 2015, doi: 10.1109/CVPR.2015.7298594.
- [52] J. Kim, J. K. Lee, and K. M. Lee, “Accurate image super-resolution using very deep convolutional networks,” *Proc. IEEE Comput. Soc. Conf. Comput. Vis. Pattern Recognit.*, vol. 2016–December, pp. 1646–1654, 2016, doi: 10.1109/CVPR.2016.182.
- [53] K. He, X. Zhang, S. Ren, and J. Sun, “Deep residual learning for image recognition,” *Proc. IEEE Comput. Soc. Conf. Comput. Vis. Pattern Recognit.*, vol. 2016–December, pp. 770–778, 2016, doi: 10.1109/CVPR.2016.90.
- [54] G. Huang, Z. Liu, L. Van Der Maaten, and K. Q. Weinberger, “Densely connected convolutional networks,” *Proc. - 30th IEEE Conf. Comput. Vis. Pattern Recognition, CVPR 2017*, vol. 2017–January, pp. 2261–2269, 2017, doi: 10.1109/CVPR.2017.243.
- [55] Z. Wang, J. Chen, and S. C. H. Hoi, “Deep Learning for Image Super-Resolution: A Survey,” vol. 43, no. 10, pp. 3365–3387, 2021.
- [56] Y. Tan *et al.*, “CrossNet++: Cross-scale Large-parallax Warping for Reference-based Super-resolution,” *IEEE Trans. Pattern Anal. Mach.*

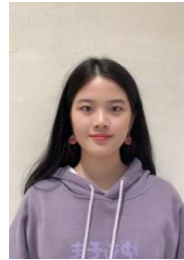
- Intell.*, vol. 8828, no. c, pp. 1–1, 2020, doi: 10.1109/tpami.2020.2997007.
- [57] Y. Wang, F. Perazzi, B. McWilliams, A. Sorkine-Hornung, O. Sorkine-Hornung, and C. Schroers, “A fully progressive approach to single-image super-resolution,” *IEEE Comput. Soc. Conf. Comput. Vis. Pattern Recognit. Work.*, vol. 2018-June, pp. 977–986, 2018, doi: 10.1109/CVPRW.2018.00131.
- [58] M. Haris, G. Shakhnarovich, and N. Ukita, “Deep Back-Projection Networks for Single Image Super-resolution,” *IEEE Trans. Pattern Anal. Mach. Intell.*, vol. 2, no. d, pp. 1–1, 2020, doi: 10.1109/tpami.2020.3002836.
- [59] Z. Li, J. Yang, Z. Liu, X. Yang, G. Jeon, and W. Wu, “Feedback network for image super-resolution,” *Proc. IEEE Comput. Soc. Conf. Comput. Vis. Pattern Recognit.*, vol. 2019-June, pp. 3862–3871, 2019, doi: 10.1109/CVPR.2019.00399.
- [60] J. Ai, G. Fan, Y. Mao, J. Jin, M. Xing, and H. Yan, “An Improved SRGAN Based Ambiguity Suppression Algorithm for SAR Ship Target Contrast Enhancement,” *IEEE Geosci. Remote Sens. Lett.*, pp. 1–5, 2021, doi: 10.1109/LGRS.2021.3111553.
- [61] H. Wang, “HFD - SRGAN: Super-Resolution Generative Adversarial Network with High-frequency discriminator,” pp. 3148–3153, 2020.
- [62] M. M. Majdabadi and S. B. Ko, “MSG-CapsGAN: Multi-Scale Gradient Capsule GAN for Face Super Resolution,” *2020 Int. Conf. Electron. Information, Commun. ICEIC 2020*, pp. 10–12, 2020, doi: 10.1109/ICEIC49074.2020.9051244.
- [63] A. Mahendran and A. Vedaldi, “Understanding deep image representations by inverting them,” *Proc. IEEE Comput. Soc. Conf. Comput. Vis. Pattern Recognit.*, vol. 07-12-June-2015, pp. 5188–5196, 2015, doi: 10.1109/CVPR.2015.7299155.
- [64] V. Lempitsky, A. Vedaldi, and D. Ulyanov, “Deep Image Prior,” *Proc. IEEE Comput. Soc. Conf. Comput. Vis. Pattern Recognit.*, pp. 9446–9454, 2018, doi: 10.1109/CVPR.2018.00984.
- [65] N. Navab, J. Hornegger, W. M. Wells, and A. F. Frangi, “Medical Image Computing and Computer-Assisted Intervention - MICCAI 2015: 18th International Conference Munich, Germany, October 5-9, 2015 proceedings, part III,” *Lect. Notes Comput. Sci. (including Subser. Lect. Notes Artif. Intell. Lect. Notes Bioinformatics)*, vol. 9351, no. Cvd, pp. 12–20, 2015, doi: 10.1007/978-3-319-24574-4.
- [66] Y. Gandelsman, A. Shocher, and M. Irani, ““Double-dip”: Unsupervised image decomposition via coupled deep-image-priors,” *Proc. IEEE Comput. Soc. Conf. Comput. Vis. Pattern Recognit.*, vol. 2019-June, no. 788535, pp. 11018–11027, 2019, doi: 10.1109/CVPR.2019.01128.
- [67] M. Nejati, S. Samavi, and S. Shirani, “Multi-focus image fusion using dictionary-based sparse representation,” *Inf. Fusion*, vol. 25, pp. 72–84, 2015, doi: 10.1016/j.inffus.2014.10.004.
- [68] H. Zhao, O. Gallo, I. Frosio, and J. Kautz, “Loss Functions for Image Restoration with Neural Networks,” pp. 1–11.
- [69] V. Baroncini, L. Capodiferro, E. D. Di Claudio, and G. Jacovitti, “The polar edge coherence: A quasi blind metric for video quality assessment,” *Eur. Signal Process. Conf.*, no. September, pp. 564–568, 2009.



Yuanjie Gu received the B.E. degree from the School of Petroleum, China University of Petroleum, China, in 2020. He is currently a master student in the Computational Optics Laboratory, School of Science, Jiangnan University, Wuxi. His current research interests include computational photography, unsupervised deep learning, image fusion, super-resolution and single molecule imaging.



Zhibo Xiao received the B.E. degree from the School of Petroleum, China University of Petroleum, China, in 2020. He is currently a master student in the Computational Optics Laboratory, School of Science, Jiangnan University, Wuxi. His current research interests include computational photography and deep learning.

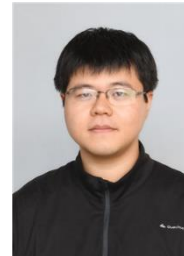


Hailun Wang received the B.E. degree from the School of Petroleum, China University of Petroleum, China, in 2021. She is currently a master student in the Computational Optics Laboratory, School of Science, Jiangnan University, Wuxi. Her current research interests include computational photography and deep learning.



Cheng Liu received the B.E. and M.E. degrees from Soochow University in 1993 and 1996, respectively, and the Ph.D. degree from Shanghai Institute of Optics and Fine Mechanics in 2003. From 2003 to 2011 he was a postdoctoral associate with Yonsei University, National University of Singapore, Gwangju Institute of Science and Technology, and University of Sheffield. Since 2011, he becomes a full professor in Jiangnan University and leads the Computational Optics Laboratory. He is also affiliated with Shanghai

Institute of Optics and Fine Mechanics. He has published more than 150 journal articles and conference papers. His current research interests include computational imaging, optical testing and microscopy.



Shouyu Wang received the B.E. and Ph.D degrees from Nanjing University of Science and Technology in 2010 and 2015. He is currently an associate professor and co-principal investigator in the Computational Optics Laboratory, School of Science, Jiangnan University, Wuxi. He is also affiliated with Single Molecule Nanometry Laboratory in Nanjing Agricultural University. He has published more than 100 journal articles and conference papers. His current research interests include computational sensing and imaging,

microscopy and single molecule techniques.